Langmuir

Article

pubs.acs.org/Langmuir

Bicontinuous Ceramics with High Surface Area from Block Copolymer Templates

Han-Yu Hsueh and Rong-Ming Ho*

Department of Chemical Engineering, National Tsing Hua University, Hsinchu 30013, Taiwan

Supporting Information

ABSTRACT: Mesoporous polymers with gyroid nanochannels can be fabricated from the self-assembly of degradable block copolymer, polystyrene-*b*-poly(L-lactide) (PS-PLLA), followed by hydrolysis of PLLA block. Well-defined polymer/ceramic nanohybrid materials with inorganic gyroid nanostructures in a PS matrix can be obtained by using the mesoporous PS as a template for sol−gel reaction. Titanium tetraisopropoxide (TTIP) is used as a precursor to give a model system for the fabrication of metal oxide nanostructures from reactive transition metal alkoxides. By controlling the rates of capillary-driven pore filling and sol−gel reaction, the templated synthesis can be well-developed. Also, by taking advantage of calcination, bicontinuous TiO_2 with controlled crystalline phase (i.e., anatase phase) can be fabricated after removal of the PS template and crystallization of TiO_2 by calcination leading to high photocatalytic efficiency. This new approach provides an easy way to fabricate high-surface-area and high-porosity ceramics with self-supporting structure and controlled crystalline phase for practical applications. As a result, a platform technology to fabricate precisely controlled polymer/ceramic nanohybrids and mesoporous ceramic materials can be established.

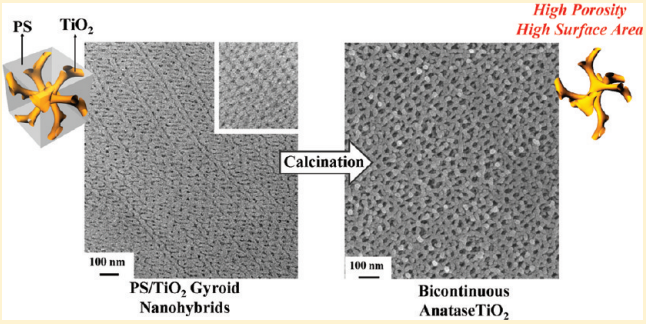

INTRODUCTION

Porous materials whose properties depend on their individual components and morphologies are potentially next-generation materials due to their excellent material characteristics, including optical, electrical, magnetic, and mechanical properties. Porous materials, such as nuclear track etched polycarbonate membrane[1] and anodized aluminum oxide films,[2] have been exploited for applications in various fields. Although AAO membranes with mesoscale pores are commercially available, their cylinder shapes may limit the applications in nanotechnologies. As for the exploitation of the opals/inverse opals,[3,4] a variety of porous morphologies might be fabricated, but the limitation of micrometer size remains. Mesoporous silica (i.e., MCM materials)[5] has thus been developed for applications. Although mesoporous silica with various framework structures and pore sizes has been successfully synthesized, this approach generally involves a multistep process and, most critically, it is difficult to acquire the production of large-size bulk and large-area continuous films. How to precisely control the geometries of the pores with nanometer-size dimension for porous materials is critical to optimizing their functions and performance in practical applications, but it remains challenging.

In recent decades, block copolymers (BCPs) have been extensively investigated because of their ability to self-assemble into one-, two-, and three-dimensional periodic nanostructures with readily adjustable size, depending on their constituted compositions and molecular weights.[6,7] Consequently, well-defined nanostructures can be tailored by the molecular engineering of synthetic BCPs with promising features for applications in nanotechnologies. Also, by taking advantage of the degradable character of BCPs, mesoporous polymer materials can be prepared by removal of constituted components in BCPs through ozonolysis,[8] UV degradation,[9] and reactive ion etch.[10] As a result, BCPs containing a degradable block have drawn considerable attention for the preparation of mesoporous polymers. Also, polylactide-containing BCPs (such as polystyrene-*b*-poly(D,L-lactide) (PS-PLA)[11] and polystyrene-*b*-poly(L-lactide) (PS-PLLA)[12,13]) are highly suited for the fabrication of mesoporous polymers because of the unstable character of ester group in polylactides, which can be hydrolytically decomposed.

Among all of the nanostructures resulting from BCP self-assembly, gyroid is one of the most appealing morphologies for practical applications because of its unique geometry, composed of a matrix and two continuous but independent, interpenetrating networks in three-dimensional space; as a result, it is also referred to as a double gyroid nanostructure.[14−16] After the selective degeneration of minor phase, the gyroid nanostructure can be exploited to create fully interconnected nanochannels. Because of high porosity and high specific surface area, the mesoporous polymers resulting

Received: March 6, 2012
Revised: April 20, 2012
Published: April 24, 2012

 © 2012 American Chemical Society dx.doi.org/10.1021/la3009706 | Langmuir 2012, 28, 8518−8529

Scheme 1. Schematic Illustration for the Creation of Well-Defined Bicontinuous TiO_2 from the Templating of BCP[a]

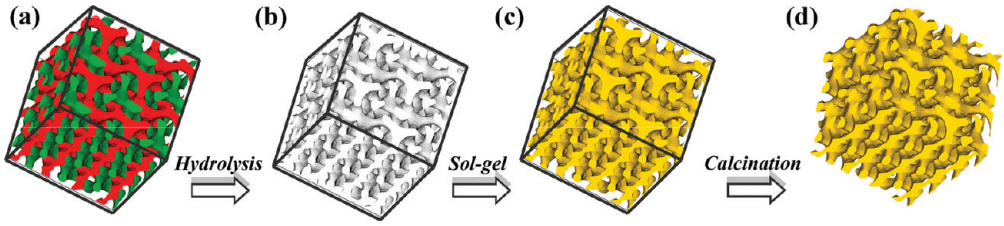

[a](a) PS-PLLA gyroid morphology (skeleton of double gyroid structure with two identical networks (green and red)). (b) Gyroid-forming mesoporous PS template after removal of minority PLLA networks. (c) PS/TiO_2 gyroid nanohybrids via templated sol-gel reaction. (d) Bicontinuous TiO_2 with crystalline phase after removal of PS template through calcination.

from the BCP gyroid are very promising for use in a variety of applications, such as photonic crystals,[17,18] catalysts,[19] ceramic membranes,[20−22] and hybrid solar cells.[23] Most interestingly, mesoporous polymers can be used as templates for templated reactions.[24−32] By exploiting the templating process (i.e., nanoreactor concept), reactions, such as electrochemical deposition,[23,25,27] electroless plating,[28] and sol−gel reaction,[29] can be carried out within the BCP templates for manufacture of mesoporous inorganic materials with precisely controlled textures after removal of polymer template. For instance, Crossland et al. reported that anatase TiO_2 gyroid network could be formed by using BCP templates for electrochemical deposition to give better performance as dye-sensitized solar cell.[23] Recently, with the combination of the self-assembly of degradable BCPs and sol−gel chemistry, we suggested a novel method for the preparation of mesoporous gyroid SiO_2 with an extremely low refractive index. Mesoporous polymers with gyroid nanochannels can be fabricated from the self-assembly of PS-PLLA followed by the hydrolysis. Well-defined PS/SiO_2 gyroid nanohybrids can be obtained by using the mesoporous polymers as templates for sol−gel reaction. After the UV degradation of the PS matrix, the nanohybrids can be transferred to a highly porous SiO_2 gyroid network with low refractive index (as low as 1.10).[29]

The sol−gel reaction is a wet-chemical technique and widely used in the fields of science and engineering.[33,34] Precursors, such as metal alkoxides and metal salts, are used to form a chemical solution (sol) for the following gelation process. After hydrolysis, which is followed by condensation reaction, the transparent solution starts to become an integrated network (gel) of either network polymers or discrete colloidal particles. The metal alkoxides with chemical formula $M(OR)_x$ are reactive when exposed to moisture, heat, or light. Notably, the templating of BCPs from reactive transition metal alkoxides, such as $Ti(OR)_4$ and $Zr(OR)_4$, is extremely difficult because of their unstable precursors in the presence of moisture, causing blockage of pore filling. As a result, for a successful templated synthesis, it is necessary to pore-fill the precursors in sol state before the occurrence of gelation resulting from substantial condensation. For the sol−gel reaction of silicon oxides, the successful templating can be well-achieved because of the extremely slow reaction rate of hydrolysis that alleviates the problem of forming large gelled aggregates resulting in blocking of the pore-filling process.[29] Herein, the formation of well-defined TiO_2 nanostructure using titanium alkoxides (i.e., titanium tetraisopropoxide, TTIP) as precursors can be achieved by adjusting the rates of pore-filling process and sol−gel reaction so as to give a model system for the fabrication of metal oxide nanostructures from reactive transition metal alkoxides. As one of the most important photocatalysts and semiconductors, TiO_2 plays an important role in the extensive development of optical, electronic, and green energy applications. Because of the strong oxidizing and reducing ability of TiO_2 under UV irradiation, TiO_2 can be used in various fields such as a semiconductor in solar cell,[23,35] photocatalysis,[36,37] sensing,[38,39] photoelectrolysis,[40,41] and photovoltaics.[42−44] Notably, the photocatalytic process, a heterogeneous process, depends on not only the intrinsic properties of the materials, but also the structural characteristics. High specific surface area and porosity of TiO_2 are highly desired for applications. High specific surface area provides abundant active sites for material exchange, and high porosity makes the transport of involved chemical species in and out of the porous structure much easier. Also, a highly ordered mesoporous TiO_2 with anatase phase may lead to better performance as compared to a disordered ones.[45] Although various nanostructured TiO_2 have been synthesized,[46−50] it is still challenging to manufacture well-defined nanostructured anatase TiO_2 with high porosity and high surface area.

Scheme 1 shows this method. PS-PLLA with a total molecular weight of 61 000 g mol^{-1} and a PLLA volume fraction of 39% was synthesized. A double gyroid phase consisting of cocontinuous PLLA networks in a PS matrix can be formed after solution casting of the synthesized PS-PLLA followed by quenching from microphase-separated melt. After hydrolytic treatment, mesoporous PS matrix can be formed, and used as a template for the sol−gel reaction. By tuning the hydrolysis and condensation for the sol−gel reaction using chelating agents, the morphological evolution of nanostructured materials from templating can be well-controlled under appropriate reaction conditions, such as pH value, temperature, and solvent used for the sol−gel reaction. Also, by taking advantage of calcination, bicontinuous TiO_2 with controlled crystalline phase (i.e., anatase phase) can be fabricated after removal of the PS template and crystallization of TiO_2 by calcination. This new approach gives rise to an easy way for fabrication of high-surface-area and high-porosity TiO_2 with self-supporting structure and controlled crystalline phase.

RESULTS AND DISCUSSION

Fabrication of Mesoporous PS Template. Figure 1a shows the TEM image of the microsection of solution-cast PS-PLLA sample after specific thermal treatment (see Experimental Section for details). The PS matrix, selectively stained with RuO_4, appears dark, whereas the PLLA microdomains appear bright. The [211] projection of the PS-PLLA suggests the formation of a gyroid phase. Corresponding one-dimensional small-angle X-ray scattering (1D SAXS) profile (Figure 2a) further confirms the observed gyroid phase with a space group

dx.doi.org/10.1021/la3009706 | Langmuir 2012, 28, 8518−8529

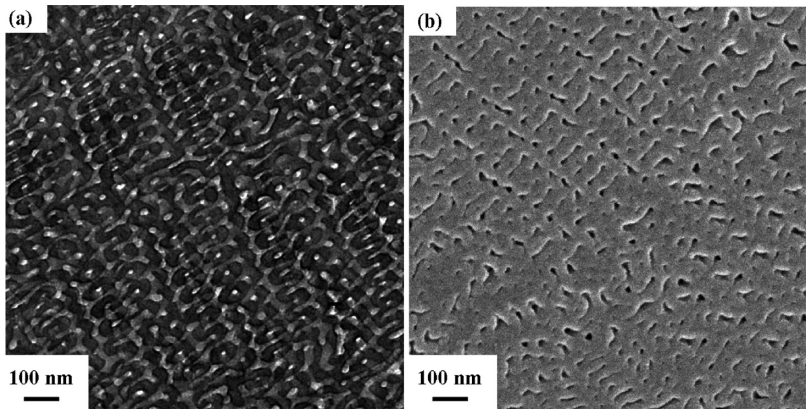

Figure 1. (a) TEM micrograph of the [211] projection of the gyroid-forming PS-PLLA with RuO_4 staining. (b) FESEM micrograph of mesoporous PS template from the gyroid-forming PS-PLLA after removal of minor PLLA networks.

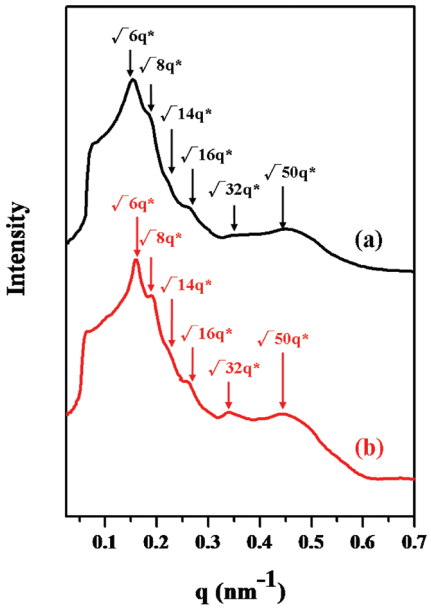

Figure 2. One-dimensional SAXS profiles of (a) gyroid-forming PS-PLLA; (b) mesoporous PS template from the gyroid-forming PS-PLLA after removal of minor PLLA networks.

of $Ia\bar{3}d$ at which scattering peaks are found at q^* ratios of $\sqrt{6}:\sqrt{8}:\sqrt{14}:\sqrt{16}:\sqrt{32}:\sqrt{50}$. The interdomain spacing of $(211)_{gyroid}$ ($d_{(211)G}$) was determined as approximately 40.9 nm from the primary reflection. The structure factor calculations of SAXS pattern for a bulk sample of PS-PLLA after thermal treatment is shown in Supporting Information Figure S1. After hydrolysis in a mild aqueous base, the PLLA block of the PS-PLLA can be removed completely (Figure 1b). Figure 2b displays the 1D SAXS profile of the PS-PLLA after hydrolysis; the diffraction peaks at the q^* ratios remain unchanged as compared to Figure 2a, reflecting the successful templating. The interdomain spacing of $(211)_G$ (i.e., $d_{(211)G}$) of the mesoporous PS template was determined to be approximately 39.8 nm from the primary reflection, indicating that there is a 2.6% shrinkage of its original size. We speculate that the change in the interdomain spacing is attributed to the cavitation effect resulting from removal of the hydrolysis solution, leading to a reduction in proportional dimension of the gyroid feature. Consequently, a PS matrix with bicontinuous nanochannels was fabricated and employed as a template for sol–gel reaction. Supporting Information Figure S2 shows the pore size distribution of the mesoporous PS templates, and the average pore size was determined as approximately 31.3 nm that is consistent to the TEM results. The porosity of the mesoporous PS templates is about 37% from N_2 adsorption experiments, and the specific surface area was calculated as 97 $m^2\ g^{-1}$. As a result, the templated results are, in principle, in line with the use of template.

Control of Pore-Filling Process and Sol–Gel Reaction for Templating. For a sol–gel reaction, it is well-known that the reaction can be carried out by acid-catalyzed and base-catalyzed reactions. While the sol–gel reaction was under base-catalyzed condition, the sol will transfer to gel with oversize dimensions resulting in blocking of the pore-filling process. Supporting Information Figure S3a shows the photos of the acid-catalyzed and base-catalyzed sol–gel precursor solutions. While the sol–gel reaction is under basic conditions, the sol will rapidly become a milky solution due to the formation of gels with sizes larger than the wavelength of visible light (namely, much larger than the pore size of the PS template). By contrast, the solution of acid-catalyzed sol–gel reaction could remain a transparent solution for a reasonable time period under ambient condition, indicating that the acid-catalyzed reaction is pertinent for following the pore-filling process.

For a successful pore-filling process in templated synthesis, appropriate solvents are required in order to enhance the wetting tendency of the precursor solution into the PS template through capillary force. Considering the hydrophobicity of the PS inner wall and the requirement of aqueous ingredients as sol, amphiphilic substances, such as acyclic alcohols, were usually used. Unlike silicon alkoxides,[29] the majority of transition metal alkoxides are very reactive even in a low-humidity environment, resulting in the formation of large gelled aggregates due to fast hydrolysis followed by condensation reaction. Consequently, the sol–gel reaction will occur before pore-filling the template resulting in the blocking of pore-filling process. It is noted that, for a transition metal alkoxide, the oxidation state of the metal is generally smaller than its normal coordination number so that it tends to increase the coordination sites and result in a stable state. For example, the TTIP monomers become unstable dimers via solvate bonds in a polar solvent such as ethanol but can be stabilized as trimers via alkoxy bridges in a nonpolar solvent such as benzene.[51] The alkoxy bridges appear to be more stable toward hydrolysis than solvate bonds. With the use of weak polar or nonpolar

dx.doi.org/10.1021/la3009706 | Langmuir 2012, 28, 8518–8529

solvents, coordination expansion of the transition metal would occur via alkoxy bridging leading to the formation of condensed oligomer molecular precursors that gives the transition metal a higher coordination number for stabilization.[33,34] Consequently, for the selection of amphiphilic substance (i.e., surfactant), it is necessary to acquire acyclic alcohols with weaker polarity for lower reactivity of the hydrolysis. According to the degradation chemistry of polylactides,[11b] there are hydroxyl groups on the surface of pore walls after hydrolysis, but the surface property should not be completely dominated by the hydroxyl chain ends. Although it is reasonable to suggest that the hydrophilicity of the PS inner wall should be enhanced because of the hydroxyl functionality, the wetting capability of the PS pore driven by capillary force should be quite different from that of hydrophilic materials. For the humidity sensitivity of precursor like TTIP, acyclic alcohols with weaker polarity, such as propanol, are commonly used for the formation of polymeric TiO_2 gel. Supporting Information Figure S3b shows the TEM micrograph of PS/TiO_2 nanohybrids prepared by acid-catalyzed sol–gel reaction using propanol as a solvent at room temperature. In contrast to Figure 1a, the contrast of the PS/TiO_2 nanohybrids without RuO_4 staining is reversed, showing the formation of the TiO_2 gel. However, the forming pore-filled TiO_2 appears as an irregular texture—a signature of incomplete templating of BCPs. The unsuccessful templating is attributed to the growth of oversize gel particles so as to limit the capability of pore-filling.

It is noted that the rate of sol–gel reaction is very sensitive to reaction temperature. To reduce the reaction rate, the sol–gel reaction was carried out in the temperature lower than room temperature. Supporting Information Figure S4a shows the TEM image of PS/TiO_2 nanohybrids from acid-catalyzed sol–gel reaction using propanol as a solvent at 5 °C. The contrast of the PS/TiO_2 nanohybrids without RuO_4 staining is reversed as compared to RuO_4-stained PS-PLLA, demonstrating that the formation of the TiO_2 gel is successful so as to give significant contrast from titanium. Nevertheless, instead of forming gyroid nanostructure with well-defined threefold symmetry, co-continuous texture with distorted nanostructured networks was observed for the PS/TiO_2 nanohybrids from the templating. Supporting Information Figure S4b shows the corresponding 1D small-angle X-ray scattering (1D SAXS) profile of the PS/TiO_2 nanohybrids. Interestingly, the characteristic primary reflections at q ratios of $\sqrt{6}$ and $\sqrt{8}$ for a gyroid phase can still be identified but are diffusive in peak intensity, and the interdomain spacing of $d_{(211)G}$ is reduced to approximately 35.1 nm in comparison with the original value of 40.9 nm. The reduction in dimension is close to 15% of its original size. On the basis of those experimental observations, we speculate that the change in the interdomain spacing is attributed to the propanol swelling of the PS matrix followed by removal of the solvent. At first, the PS template was swollen and softened by propanol resulting in gyroid-like morphology with distorted texture. Consequently, volume shrinkage will occur during the evaporation of the solvent due to kinetic origin, as evidenced by the broadening of primary reflections and the smearing of high-order scattering.

Chelating Agent for Sol–Gel Reaction. To reduce the degree of propanol swelling of the PS templates, acyclic alcohols with stronger polarity, such as methanol, should be used as solvents for the templated sol–gel reaction. Nevertheless, it is in conflict with the requirement of acyclic alcohols with lower polarity as mentioned above. Precipitation would occur immediately even with high loading of methanol, indicating that the hydrolysis rate is still too fast to fulfill the pore-filling criteria by using methanol. Chelating agents, such as acetylacetone (AcAc) and diethanolamine (DEA), are commonly used to reduce the hydrolysis rate. AcAc is a typical α-diketone that can be ionized in aqueous solution as a weak acid. Considering the prerequisite of an acid-catalyzed sol–gel reaction for templating of BCPs, AcAc was chosen as a chelating agent. Although AcAc is a suitable chelating agent for the TTIP in the sol–gel reaction, the nanostructure from the templating of BCP still encounters the distortion problem. It is noted that the keto and enol forms of AcAc may coexist in solution. As a result, the existence of keto form of AcAc might cause swelling of the PS template resulting in distortion of the templated morphologies (see Supporting Information Figure S5 for details). The PS template would be swollen by AcAc for a long reaction time even at low loading of AcAc that would cause distortion of the nanostructures, and the problem becomes much more serious at high loading of AcAc.

To alleviate the swelling problem, DEA was thus used as chelating agent by considering its stability in precursor solution. It is noted that DEA acts as a weak base like other organic amines. As a result, the loading content of DEA should be balanced by the introduction of acid catalysts to maintain the pH value below 4. So, a higher molar concentration of $HCl_{(aq)}$ was used for the templated synthesis so as to give a linear step polymerization of metal alkoxides. Figure 3a shows the TEM image of PS/TiO_2 gyroid nanohybrids from templated sol–gel reaction using DEA (DEA/TTIP mole ratio of 0.5) as a chelating agent in methanol at 5 °C. The formation of well-defined PS/TiO_2 gyroid nanohybrids can be achieved, as evidenced by the well-ordered projections from TEM observations with [211] and [220] projections at which the specific bicontinuous nanostructure with threefold axes of symmetry can be clearly identified. Figure 3b displays the corresponding 1D SAXS profile. Consistent with the TEM results, the scattering profile at q ratios of $\sqrt{6}:\sqrt{8}:\sqrt{24}$ suggests the formation of well-ordered PS/TiO_2 gyroid nanohybrids. On the basis of the two characteristic primary peaks for the nanohybrids at a q ratios of $\sqrt{6}$ and $\sqrt{8}$, the interdomain spacing is reduced to approximately 36.4 nm. Also, the q ratio of $\sqrt{6}:\sqrt{8}:\sqrt{24}$ is quite different from that of the intrinsic PS-PLLA and the mesoporous PS template with the q ratio of $\sqrt{6}:\sqrt{8}:\sqrt{14}:\sqrt{16}:\sqrt{32}:\sqrt{50}$. We speculate that the reduction in the interdomain spacing is attributed to slight swelling of the PS matrix by methanol and the formation of TiO_2 dry gel leads to a reduction in proportional dimension of the gyroid feature over the aging period. Also, the variation in q ratios might be attributed to the changes resulting from different electron density contrast and the form factor of TiO_2 microdomains. Note that the TiO_2 microdomain from the sol–gel reaction consists of TiO_2 nanoparticles so that the packing of those nanoparticles and their size and shape should be critical to the electron density contrast in the synthesized nanohybrids so as to affect the form factor as well. Detailed examination of the variations is still in progress. To further explore the effect of the chelating agent, systems with higher DEA loading were examined. Figure 3c shows the corresponding 1D SAXS profiles of PS/TiO_2 gyroid nanohybrids synthesized using higher loading of DEA at the molar ratio of DEA/TTIP of 1.0. The q ratios are the same with Figure 3b, suggesting that the preservation of the nanostructure from the templating of BCP is not dependent upon the loading level of

dx.doi.org/10.1021/la3009706 | Langmuir 2012, 28, 8518–8529

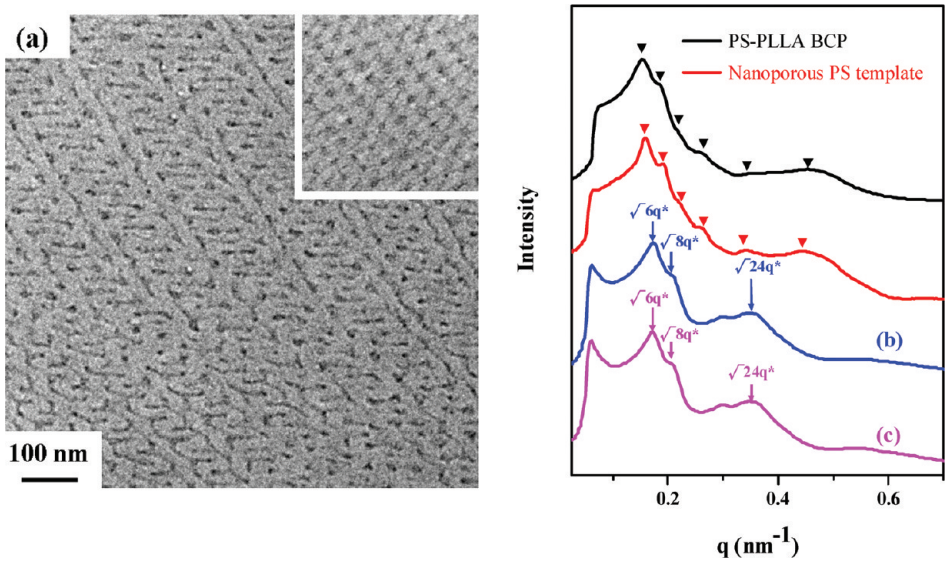

Figure 3. (a) TEM micrograph of the [211] projection of the PS/TiO_2 gyroid nanohybrids without staining. The acid-catalyzed sol–gel reaction was performed using DEA (DEA/TTIP mole ratio of 0.5) as a chelating agent in methanol at 5 °C. The inset shows the [220] projection of the double gyroid morphology. Corresponding 1D SAXS profiles of the PS/TiO_2 gyroid nanohybrids by using DEA as a chelating agent with DEA/TTIP mole ratio of (b) 0.5 and (c) 1.0 in methanol at 5 °C.

DEA, unlike the case using the AcAc as chelating agent. The structure factor calculations of SAXS pattern for the PS/TiO_2 gyroid nanohybrids are shown in Supporting Information Figure S6. As a result, a well-defined TiO_2 double gyroid network in a PS matrix can be formed by carrying out acid-catalyzed sol–gel reaction at low temperature using DEA as chelating agent within the gyroid nanochannels. The experimental details and procedures for the fabrication of well-ordered polymer/ceramic nanohybrids from BCP templates are summarized in Figure 8.

Fabrication of Bicontinuous TiO_2. The PS/TiO_2 gyroid nanohybrids were further treated by exposure to UV light under atmospheric condition for 24 h with a UV source (wavelength = 254 nm and intensity = 3 mW/cm^2) to remove the PS matrix. Fourier transform infrared spectroscopic (FT-IR) was used to confirm that the PS template can be completely removed after UV irradiation. Figure 4 shows the FESEM image of the texture of the bicontinuous TiO_2. It is noted that TiO_2 occurs in nature in three different forms: rutile, anatase, and brookite. Although rutile is the most common form of stable crystalline TiO_2, anatase shows the best photocatalytic efficiency so that the TiO_2 with anatase crystalline phase is extensively applied in industry for applications. Notably, the TiO_2 synthesized by the sol–gel process is usually amorphous. Figure 5a shows the corresponding wide-angle X-ray scattering (WAXS) pattern of the bicontinuous TiO_2, reflecting the formation of amorphous TiO_2 after the sol–gel reaction

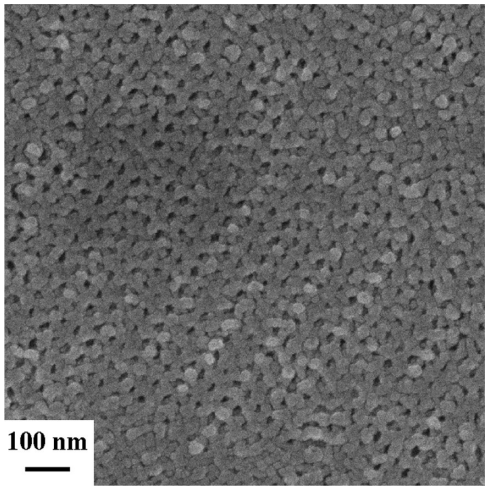

Figure 4. FESEM micrograph of bicontinuous TiO_2 from the PS/TiO_2 gyroid nanohybrids after removal of the PS template by exposure to UV light under atmospheric condition without calcination.

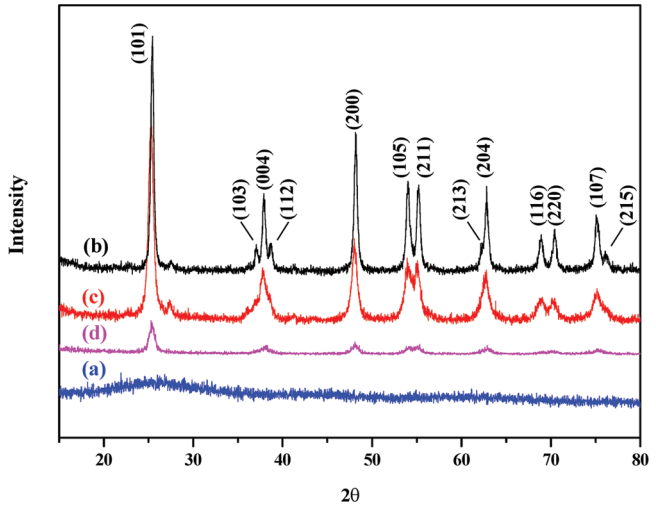

Figure 5. 1D WAXS profiles of the bicontinuous TiO_2 with different thermal treatments: (a) without any calcination; (b) ramped from 25 to 450 °C at 0.5 °C min^{-1}, held at 450 °C for 2 h, and then cooled from 450 to 25 °C at 0.5 °C min^{-1}; (c) ramped from 25 to 450 °C at 10 °C min^{-1}, held at 450 °C for 2 h, and then cooled from 450 to 25 °C at 10 °C min^{-1}; (d) ramped from 25 to 300 °C at 3 °C min^{-1}, held at 300 °C for 12 h, then ramped from 300 to 450 °C at 3 °C min^{-1}, held at 450 °C for 3 h, and then cooled from 450 to 25 °C at 3 °C min^{-1}.

dx.doi.org/10.1021/la3009706 | *Langmuir* 2012, 28, 8518–8529

followed by UV degeneration of the PS template. To acquire crystalline TiO_2, in particular with anatase form, for practical applications, further thermal treatment was thus carried out.

Calcination is a common thermal treatment that can be used to increase the crystallinity so as to improve the densification of TiO_2. Also, ceramics obtained by the sol−gel reaction are microporous materials with pore size ranging from 0.3 to 3 nm, resulting from removal of solvent after the sol−gel reaction. To increase the crystallinity and initiate densification, precise control of the crystallization behavior during calcination is necessary. Note that the calcination of amorphous TiO_2 from the templated sol−gel reaction is still challenging, since the crystallization of TiO_2 at high temperature (usually above 450 °C) will easily cause the collapse of the pores, in particular, with nanometer size. Moreover, to acquire the TiO_2 with anatase phase requires well-controlled calcination conditions, such as control of sequential heating stages and corresponding heating rates, as well as calcination temperature, giving the removal of the PS template without damage to the templated morphologies. To initiate the decomposition of PS and the crystallization of TiO_2, the PS/TiO_2 gyroid nanohybrids were treated at temperature over 400 °C, and the anatase phase can be obtained after calcination. Nevertheless, the rutile phase appeared once the calcination temperature reached 600 °C (results not shown). As a result, to acquire bicontinuous TiO_2 with pure anatase phase and also to degenerate the PS template, the PS/TiO_2 gyroid nanohybrids were calcined at 450 °C in the air. Furthermore, to alleviate the possible distortion of crystallized nanohybrids from thermal expansion and cooling shrinkage, calcination was conducted by reasonably slow heating and cooling processes.

The calcination condition with slow heating and cooling processes was performed in the air using the following protocol: samples were slowly heated from 25 to 450 °C at 0.5 °C min^{-1}; held at 450 °C for 2 h, and then slowly cooled from 450 to 25 °C at 0.5 °C min^{-1}. Figure 5b shows the corresponding WAXS profile of the bicontinuous TiO_2 after the thermal treatment. All the diffractions can be indexed as tetragonal anatase with lattice constant a = 3.785 Å and c = 9.513 Å, JCPDS card no. 21−1272, corresponding to (101), (103), (004), (112), (200), (105), (211), (213), (204), (116), (220), (107), and (215) reflections, respectively. Note that significant distortion of the bicontinuous TiO_2 might occur while the cooling process is too fast to preserve the mesoporous texture. Supporting Information Figure S7a displays the FESEM micrograph of TiO_2 nanostructures from the PS/TiO_2 gyroid nanohybrids after removal of the PS template by calcination with slow heating and cooling processes. The texture of the gyroid-forming morphology has deteriorated. We speculate that the deterioration of templated nanostructure is attributed to the occurrence of significant TiO_2 crystallization. To alleviate the crystallization effect on templated morphology, a fast heating process for thermal treatment was performed in air using the following protocol: samples were rapidly heated from 25 to 450 °C at 10 °C min^{-1}; held at 450 °C for 2 h, and then rapidly cooled from 450 to 25 °C at 10 °C min^{-1}. Supporting Information Figure S7b displays the FESEM micrograph of TiO_2 nanostructures from PS/TiO_2 gyroid nanohybrids after calcination with fast heating and cooling processes. Figure 5c shows the corresponding 1D WAXS pattern of prepared bicontinuous TiO_2 at which the crystallinity of TiO_2 can be largely reduced. Nevertheless, in comparison with the results in Supporting Information Figure S7a, there are many cracks forming as indicated with a white arrow even though the embryonic form of gyroid nanostructure with threefold axes of symmetry still can be recognized. We speculate that the forming cracks might be attributed to shrinkage of the mesopores with different sizes inside the gel network resulting in inconsistency in thermal expansion and cooling shrinking of the materials in response to the heating and cooling processes.

As a result, a specific thermal treatment was performed in the air using the following protocol: PS/TiO_2 gyroid nanohybrids were heated from 25 to 300 °C at 3 °C min^{-1}, held at 300 °C for 12 h for the densification of TiO_2, then further heated to 450 °C at 3 °C min^{-1}, held at 450 °C for 3 h to remove the PS template and initiate the crystallization of amorphous TiO_2 to form anatase nanocrystals, and then cooled from 450 to 25 °C at 3 °C min^{-1}. As shown in the corresponding 1D WAXS profile of the bicontinuous TiO_2 (Figure 5d), the reflections are in line with the crystallites of TiO_2 anatase phase, but the crystallinity is reduced, whereas amorphous profile is diminished. Figure 6 shows the FESEM micrograph of the bicontinuous TiO_2 with well-defined networks. No cracks are observed so that the crystallization effect on the templated morphology is successfully alleviated. Also, the inset of Figure 6 shows the photograph of the bicontinuous TiO_2, demonstrating the fabrication of a centimeter-sized crack-free sample. The structure of the bicontinuous TiO_2 can be further identified by SAXS (Figure 7); the diffraction peaks are at q^* ratios of $\sqrt{2}:\sqrt{6}:\sqrt{8}:\sqrt{12}$. In contrast to the scattering results of the PS/TiO_2 gyroid nanohybrids, the $\sqrt{2}$ peak can be clearly identified; our previous studies suggested that the appearance of the $\sqrt{2}$ peak is attributed to the formation of a pseudosingle gyroid nanostructure with a space group of $I4_132$.[29] Although the characteristic reflections for the bicontinuous TiO_2 at high q range are relatively broad because of the deformation and collapse of the nanopores after calcination, the bicontinuous TiO_2 with long-range order (as evidenced by SAXS results) can be obtained. As a result, free-standing, bicontinuous TiO_2 can be successfully fabricated to give precisely controlled anatase TiO_2 with high porosity and high surface area. Note that the anatase TiO_2 with fine grains exhibits better mechanical

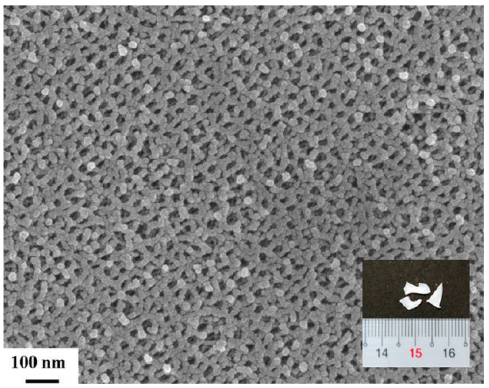

Figure 6. FESEM micrograph of bicontinuous TiO_2 from the PS/TiO_2 gyroid nanohybrids after removal of the PS matrix by specific calcination process. The inset shows the photograph of centimeter-sized bicontinuous TiO_2 bulks.

dx.doi.org/10.1021/la3009706 | Langmuir 2012, 28, 8518−8529

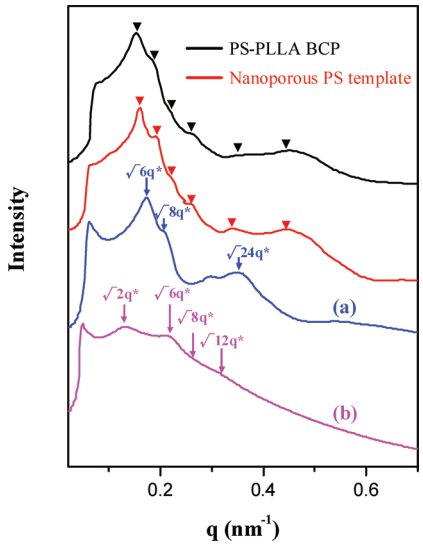

Figure 7. 1D SAXS profiles of (a) PS/TiO_2 gyroid nanohybrids. (b) Bicontinuous TiO_2 from PS/TiO_2 gyroid nanohybrids after removal of PS template after calcination.

strength and photocatalytic efficiency than the amorphous ones leading to wide applications.[52]

A brief summary about a suggested mechanism for templated sol–gel reaction is given as followings: To fabricate well-ordered polymer/ceramic nanohybrids from templating of BCPs, controlled factors, including pH value, temperature, and solvent used for templated sol–gel reaction, from reactive transition metal alkoxides should be justified. To adjust the rates of pore-filling process and sol–gel reaction, pore filling should be performed before the growth of oversized gels. As a result, an acid-catalyzed sol–gel reaction is carried out (pH value below 4) to yield primary linear polymers with minor randomly branched polymers, whereas oversized gels would be formed at high pH value. Also, to reduce the reaction rate for linear polymer chains, the sol–gel reaction should be carried out at low temperatures. On the basis of experimental results, the optimized reaction temperature is in the range 0–10 °C. Considering the pore-filling process for hydrophobic PS template and suitable solvents for metal alkoxides, acyclic alcohols were used as surfactants for pore-filling process by capillary force (i.e., wetting) and solvents for templated sol–gel reaction. To reduce the degree of swelling of the PS template, acyclic alcohols with stronger polarity such as methanol were thus used for the templated reaction. Nevertheless, it is inevitable to encounter the problem of fast hydrolysis and condensation rates of transition metal alkoxides due to the increase on polarity so that precipitation may occur immediately. To form linear polymer chains for the pore-filling process, an acid chelating agent (i.e., AcAc) should be used. A tautomeric equilibrium between keto and enol forms would occur for AcAc in acyclic alcohol solvents, and the PS template might be swollen by the keto form resulting in distorted texture of the gyroid-like nanostructure. To alleviate the swelling problem, a base chelating agent (i.e., DEA) was thus used. As a result, a well-defined bicontinuous ceramic double gyroid network in a polymeric matrix can be successfully fabricated via an acid-catalyzed sol–gel reaction by using a suitable chelating agent in methanol at low-temperature condition. Furthermore, a calcination process can be performed to remove the polymer template so as to prepare mesoporous ceramics with crystalline phase. To alleviate the crystallization effect on templated morphology and the distortion from the thermal expansion and cooling shrinkage, a specific thermal treatment should be performed. As a result, free-standing, mesoporous ceramics with high crystallinity can be successfully fabricated after the calcination process (see Supporting Information Figure S8 for details).

Photocatalytic Efficiency of Bicontinuous TiO_2. One of the well-known characteristics of nanostructured TiO_2 is the photocatalytic property of its organic component, such as in viruses, bacteria, fungi, algae, and cancer cells, which can be totally degraded and mineralized to CO_2, H_2O, and harmless inorganic anions.[52,53] Also, the corresponding photocatalytic efficiency is strongly dependent upon the surface area and the porosity of the TiO_2 for photocatalytic reaction. Obviously, the performance of the bicontinuous TiO_2 fabricated in this study will be appealing in this aspect. To demonstrate the advantage of using the bicontinuous TiO_2 for application, the analyses of the surface area and the porosity of the bicontinuous TiO_2 were determined by measuring the N_2 adsorption–desorption isotherm. The free-standing, bicontinuous TiO_2 with high crystallinity was fabricated after the specific calcination process. Figure 9a shows a combination of typical type-I and type-IV isotherms (BDDT classification).[54] In the range of low relative pressure (below 0.3), the isotherm exhibits high adsorption, indicating the presence of micropores (type-I isotherm) in the bicontinuous TiO_2. We speculate that the formation of the micropores, as evidenced by the pore size distribution result calculated by using the BJH method (Figure 9b), is attributed to the evaporation of solvent from sol–gel reaction as described previously. Micropores with average pore size below 5 nm can be found, as indicated with an arrow in Figure 9b. Also, the curve exhibits two hysteresis loops in the high relative pressure region from 0.35 to 1 (type-IV isotherms), indicating bimodal pore-size distribution in the bicontinuous TiO_2. The hysteresis loop in the relative pressure between 0.8 and 1.0 is close to a type H1 in which both the adsorption–desorption branches are nearly vertical, and they are also parallel to each other, indicating that the bicontinuous TiO_2 possesses ordered texture with uniform pores. Figure 9b shows the pore size distribution, and the average pore size was determined as approximately 24 nm, consistent with the FESEM results. Moreover, there is a small population (less than 15%) of mesopores with an average pore size of 11 nm, as calculated on the basis of the hysteresis loop in the relative pressure between 0.4 and 0.6. This hysteresis loop can be referred to a type H2, suggesting the existence of randomly distributed mesopores with smaller average pore size due to the deformation and collapse of the mesopores after calcination. Regarding the occurrence of narrow pore size distribution, we speculate that it might be attributed to the displacement of two TiO_2 networks leading to the formation of a pseudo-single gyroid network. The study of the transformation mechanism is still in progress. These results demonstrate the existence of bicontinuous TiO_2 with multi-length-scale pores. The BET specific surface area of the bicontinuous TiO_2 is 257 m^2 g^{-1}, significantly higher than the results from regular mesoporous TiO_2. The porosity of the bicontinuous TiO_2 is about 51%. As a result, the bicontinuous anatase TiO_2 with extremely high specific surface area and high porosity will be expected to possess high photocatalytic efficiency.

A simple way to examine the photocatalytic efficiency is to use methylene blue (MB) under UV irradiation (365 nm) for

dx.doi.org/10.1021/la3009706 | Langmuir 2012, 28, 8518–8529

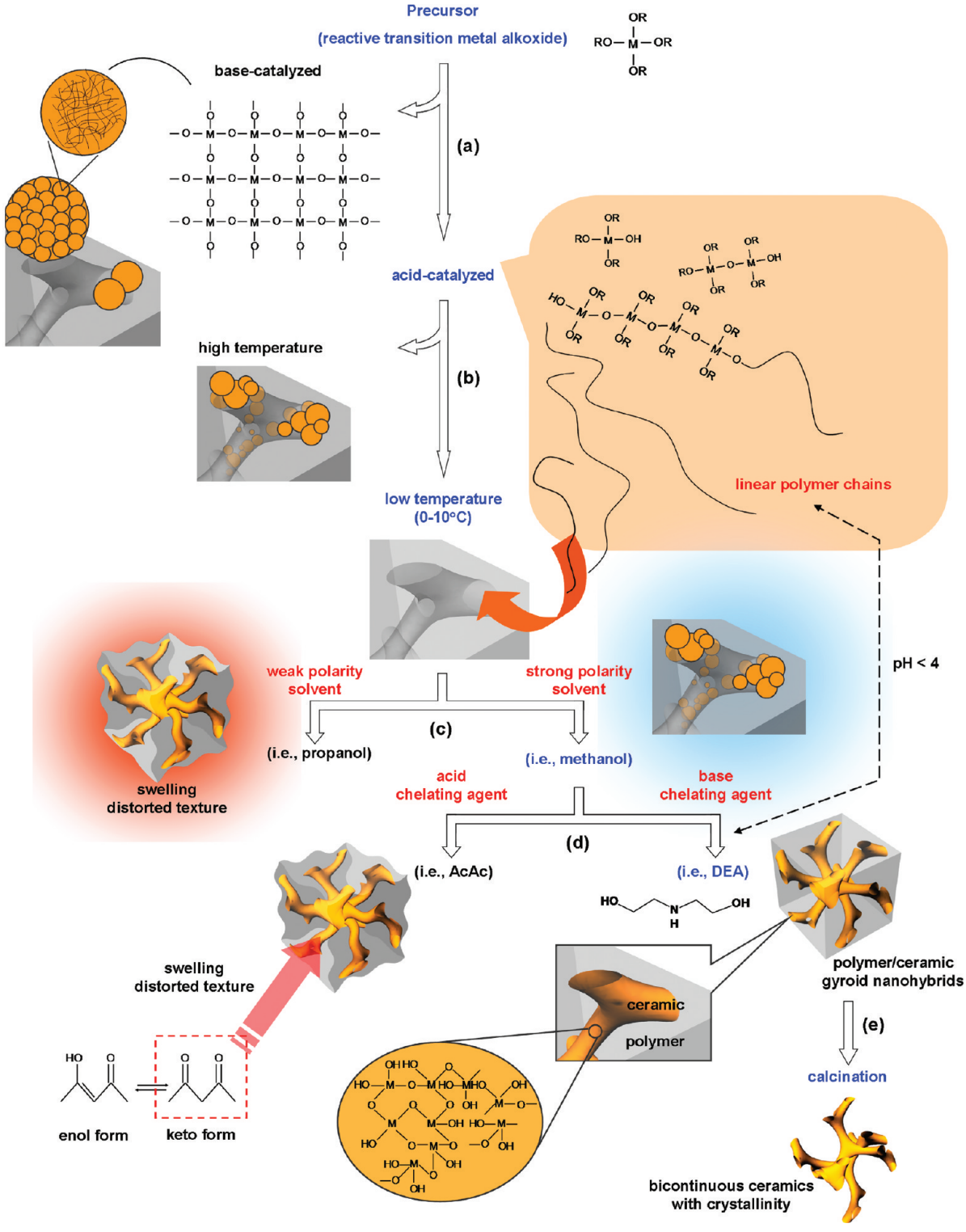

Figure 8. Schematic illustration of the creation of well-defined bicontinuous ceramics from templating of BCPs: (a) templated sol−gel reaction under acid-catalyzed or base-catalyzed precursor solutions; (b) acid-catalyzed sol−gel reactions performed at different temperatures; (c) acid-catalyzed sol−gel reaction performed in acyclic alcohols with different polarity at low temperature; (d) acid-catalyzed sol−gel reaction performed by using different chelating agents in acyclic alcohols with strong polarity (i.e., methanol) at low temperature; (e) polymer/ceramic gyroid nanohybrids resulting from acid-catalyzed sol−gel reaction performed by using suitable chelating agent (i.e., DEA) in methanol at low temperature. After a specific calcination process, free-standing, bicontinuous ceramics with high crystallinity and surface area can be successfully fabricated.

the evaluation of photocatalytic activity of the bicontinuous TiO_2 through the degradation of the MB. The MB is a basic dye of thiazine group and yields a blue solution when dissolved in water. Supporting Information Figure S8 shows the UV−vis absorption spectra of pure aqueous solution of the MB, indicating two strong absorption bands in the visible spectral

dx.doi.org/10.1021/la3009706 | *Langmuir* 2012, 28, 8518−8529

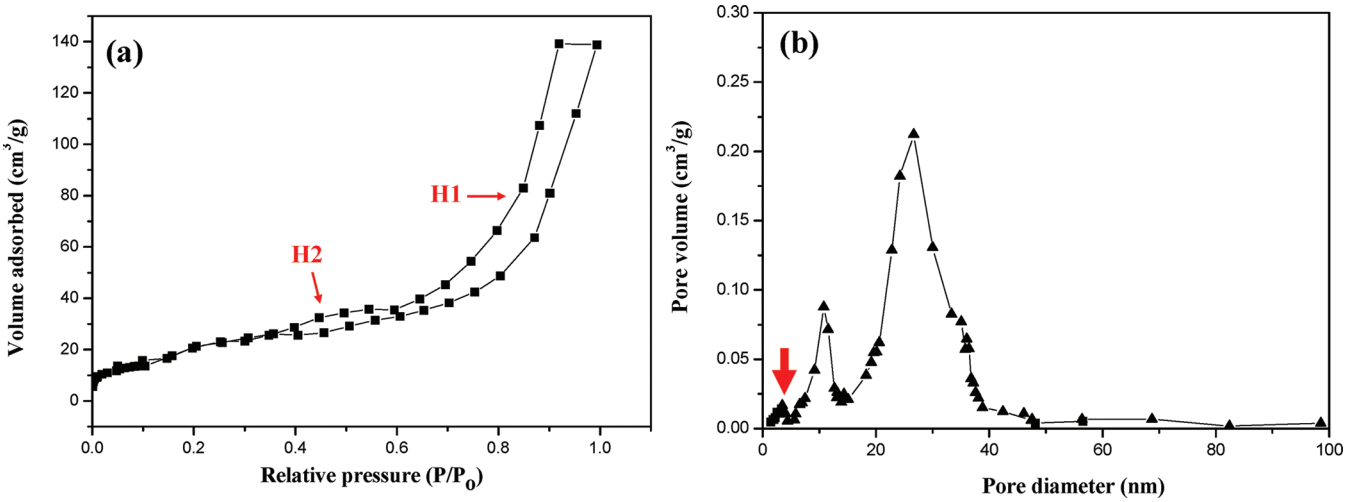

Figure 9. (a) N_2 adsorption−desorption isotherm with hysteresis loops, indicating the mesoporous property of the bicontinuous TiO_2. (b) Pore size distribution of the bicontinuous TiO_2 calculated from the adsorption branch using the BJH method. Two major pore distributions with maxima around 11 and 24 nm pore size can be identified.

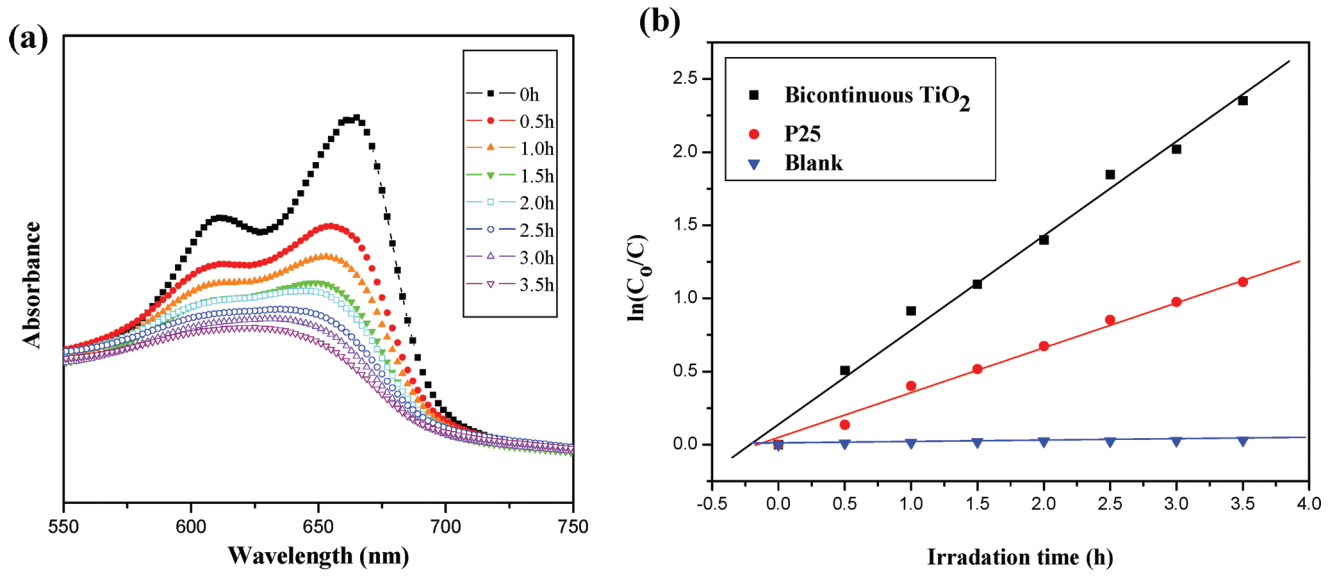

Figure 10. (a) UV−vis absorption spectra of MB solution catalyzed by the bicontinuous TiO_2 for different irradiation time. (b) Comparison of the photodecomposition rate of the MB in the presence of bicontinuous TiO_2 (□); commercial P25 TiO_2 powders (□); and blank tests (material without TiO_2 (▼)).

region at 610 and 660 nm, and a weak one in the UV region at 293 nm. The kinetics of the photodecomposition reaction can be evaluated by the following equation:

$$-\ln\frac{C}{C_o} = -\ln\left(\frac{A}{A_o}\right) = kt \quad (1)$$

where C_o and C are the concentrations of the MB before and after UV irradiation. A_o and A are the absorbances at 365 nm measured before and after UV irradiation, respectively. t is the UV irradiation time and k is the rate constant. Therefore, the absorbance changes at absorption maximum (660 nm) of the MB were measured every 30 min to determine the photocatalytic activity toward the degradation of the MB under the UV irradiation.

Figure 10a shows the UV−vis absorption spectra of the MB solution photocatalyzed by bicontinuous TiO_2 for different irradiation times. Owing to the photocatalytic property of the bicontinuous TiO_2, the initial blue color of the MB was effectively decolorized within 4 h. To further examine the photocatalytic activity of the bicontinuous TiO_2, commercial P25 TiO_2 photocatalysts were used for comparison. Figure 10b presents the degradation trend of the MB as the logarithms of normalized MB concentration against the UV irradiation time. Without using TiO_2 photocatalyst (blank test), the decomposition of the MB is almost negligible under UV irradiation. The decomposition rate of the MB becomes significant by introducing the TiO_2 photocatalysts into the MB solution, and the linear shape of the curves suggests first-order kinetics of the decomposition reaction. The reaction rate constant of commercial P25 TiO_2 powders is 0.355 48 h^{-1}. By contrast, use of the bicontinuous TiO_2 for the decomposition of the MB gives rise to the significant increase of the photocatalytic efficiency, and the reaction rate constant is 0.645 59 h^{-1} (about two times higher than commercial P25 TiO_2 powders). Notably, the photocatalytic performance of TiO_2 is determined

dx.doi.org/10.1021/la3009706 | Langmuir 2012, 28, 8518−8529

by many factors, such as surface area, pH value of environment, crystalline structure, and diffusion rate. Among the factors, crystalline structure and surface area are considered to be the critical ones. In contrast to commercial P25 TiO_2 powders, the high efficiency of the bicontinuous TiO_2 can be attributed to its bicontinuous nanostructure with extremely high surface area and high porosity leading to facilitating the adsorption of solution contaminants and effective utilization of UV light. In contrast to the powder-type commercial TiO_2, the bicontinuous TiO_2 as self-supporting bulk sample gives rise to a specific advantage for the recovery after uses. As demonstrated by the high photocatalytic efficiency of the bicontinuous TiO_2, the mesoporous TiO_2 with bicontinuous texture is appealing in the applications requiring self-supporting materials with high specific area and porosity, such as solar cell and wastewater treatment.

CONCLUSIONS

Mesoporous polymers with gyroid nanochannels can be fabricated from the self-assembly of degradable BCP, PS-PLLA, followed by the hydrolysis of PLLA blocks. Well-defined polymer/ceramic nanohybrid materials with inorganic gyroid nanostructure in a PS matrix can be obtained by using the mesoporous PS as a template for sol−gel reaction. By adjusting the rates of pore-filling process and sol−gel reaction, the formation of well-defined TiO_2 nanostructure using titanium alkoxides (i.e., titanium tetraisopropoxide, TTIP) as precursors can be achieved at which the morphological evolution of nanostructured materials from templating can be well-controlled by tuning the hydrolysis and condensation for the sol−gel reaction using chelating agents under appropriate reaction conditions, such as pH value, temperature, and solvent used, so as to demonstrate the feasibility of templated sol−gel reaction for reactive transition metal alkoxides from block copolymer templates. Also, by taking advantage of calcination, bicontinuous TiO_2 with controlled crystalline phase (i.e., anatase phase) can be fabricated after removal of the PS template and crystallization of TiO_2. The bicontinuous TiO_2 shows high photocatalytic efficiency as evidenced by the decomposition experiment of the MB. This new approach gives rise to an easy way to fabricate high-surface-area and high-porosity TiO_2 with self-supporting structure and controlled crystalline phase for practical applications. Also, it is noted that functional mesoporous ceramics, such as $BaTiO_3$, $PbTiO_3$, and ZrO_2, can also be fabricated from BCP templates via sol−gel reaction of transition metal alkoxides. Furthermore, mesoporous ceramics can be used as templates for the following reactions so as to manufacture various nanohybrid materials for applications, such as hybrid solar cells, batteries, fuel cells, and catalytic devices where a large and controlled internal surface is required. As a result, a platform technology to fabricate precisely controlled polymer/ceramic nanohybrids and mesoporous ceramic materials can be established for practical applications in nanotechnologies.

EXPERIMENTAL SECTION

Synthesis of PS-PLLA BCPs. The PS-PLLA was prepared by a sequential living polymerization using a double-headed initiator. Detailed synthetic routes of the PS-PLLA sample were described in our previously published results.[13,29] The number-average molecular weight and the molecular weight distribution (i.e., polydispersity index) of the PS were determined by GPC. The polydispersity index (PDI) of PS-PLLA was determined by GPC and the numbers of L-LA repeating units versus styrene repeating units were determined by ^1H NMR analysis. The number-average molecular weights of the PS, the PLLA, and the PDI of the PS-PLLA are 34 000 g mol^{-1}, 27 000 g mol^{-1}, and 1.21, respectively. The volume fraction of PLLA, f_{PLLA}^{v}, is thus calculated as 0.39 by assuming that the densities of PS and PLLA are 1.02 and 1.248 g cm^{-3}, respectively.

Sample Preparation. Bulk samples of PS-PLLA were prepared by solution casting from dichloromethane (CH_2Cl_2) solution (10 wt % of PS-PLLA with PLLA volume fraction, f_{PLLA}^{v} = 0.39) at room temperature for two weeks, and then dried in a vacuum oven at 65 °C for three days. The dry samples were first heated to the maximum annealing temperature, T_{max} = 185 °C for three minutes to eliminate the PLLA crystalline residues that were formed during the preparation procedure. After quenching from the microphase-separated, ordered melt at 185 °C, the samples were prepared for SAXS experiments and then sectioned by ultramicrotome (thickness ∼100 nm) for TEM observation. The microsections were stained by exposing to the vapor of a 4% aqueous RuO_4 solution for one hour. The RuO_4 attacks the double bonds in the PS blocks, rendering those microphase-separated domains dark in TEM due to the mass−thickness contrast. Then, the PLLA blocks of the PS-PLLA bulk samples were removed by hydrolysis, using a 0.5 M basic solution that was prepared by dissolving 2 g of sodium hydroxide in a 40/60 (by volume) solution of methanol/water. After three days of hydrolysis, the hydrolyzed samples were rinsed using a mixture of DI water and methanol, and then used as templates for the following sol−gel reaction.

Templated Sol−Gel Reaction. To prepare the PS/TiO_2 gyroid nanohybrids, the TiO_2 precursor, titanium tetraisopropoxide (TTIP), was introduced into mesoporous PS templates by immersing the PS templates in a bottle of TTIP/$HCl_{(aq.)}$(1 M)/methanol mixture (weight ratio = 10/1/25) with a cap to avoid moisture at room temperature for three days. TTIP, $HCl_{(aq.)}$, and methanol were used as TiO_2 precursor, catalyst, and solvent, respectively. Also, chelating agents, such as diethanolamine (DEA) and acetylacetone (AcAc), were used to form complexes with transition metal alkoxides so as to dramatically lower the sol−gel reaction rate, in particular, the corresponding hydrolysis rate. The generation of steric strain on those chelated compounds is significant to reduce the probability for reaction. After the pore-filling process of the precursor mixture, moisture was introduced into the bottle for the sol−gel reaction. The bottle without the cap was placed in an oven with controlled humidity at 50 °C for two days. Consequently, the pore-filled liquid precursor mixture can be transferred to a glassy solid (gels). After drying under atmosphere at 50 °C for one day, PS/TiO_2 gyroid nanohybrids were prepared. To fabricate amorphous bicontinuous TiO_2, the PS matrix of the PS/TiO_2 gyroid nanohybrids was degenerated by exposure to UV with a wavelength of 254 nm and an intensity of 3 mW/cm^2 for one day. Fourier transform infrared spectroscopic (FT-IR) was used to confirm that the PS matrix was completely removed after UV irradiation. Furthermore, to acquire bicontinuous TiO_2 with an anatase phase, a calcination process was performed in air using the following protocol: PS/TiO_2 gyroid nanohybrids were ramped from 25 to 300 °C at 3 °C min^{-1}; held at 300 °C for 12 h to make degradation of PS matrix and densification of TiO_2 ; then ramped from 300 to 450 °C at 3 °C min^{-1}; held at 450 °C for 3 h to remove PS matrix completely and to crystallize amorphous TiO_2 to anatase nanocrystals, and then slowly cooled from 450 to 25 °C at 3 °C min^{-1}.

Photocatalytic Efficiency of Bicontinuous TiO_2. Methylene blue (MB) was used as the model contaminant in aqueous solution. TiO_2 photocatalyst (0.015 g) including commercial P25 TiO_2 powders and the prepared bicontinuous TiO_2 were immersed into a 30 μm MB solution (100 mL) stirred for 24 h at room temperature in the dark. Consequently, the MB solutions with TiO_2 photocatalysts were irradiated with UV light (UVGL-25, UVP) centered at 365 nm with an intensity of 720 μW cm^{-2}. The test samples were under normal incidence with a distance of 3 cm to the UV light. The change of the MB concentration with radiation time was monitored by measuring the UV−vis spectra and comparing the absorbance measured at 660 nm.

dx.doi.org/10.1021/la3009706 | Langmuir 2012, 28, 8518−8529

Characterization. Small-angle X-ray scattering (SAXS) experiments were conducted at the synchrotron X-ray beamline X27C at the National Synchrotron Radiation Research Center (NSRRC) in Hsinchu. The wavelength of the X-ray beam was 0.155 nm. A MAR CCD X-ray detector (MAR USA) was used to collect the two-dimensional (2D) SAXS patterns. One-dimensional (1D) linear profile was obtained by integration of the 2D pattern. The scattering angle of the SAXS patter was calibrated using silver behenate, with the first-order scattering vector q^* ($q^* = 4\lambda^{-1} \sin\theta$, where 2θ is the scattering angle) being 1.076 nm^{-1}. Bright-field transmission electron microscopy (TEM) images were obtained using the mass−thickness contrast with a JEOL JEM-2100 LaB6 transmission electron microscope (at an accelerating voltage of 200 kV). Field-emission scanning electron microscopy (FESEM) observations were performed on a JEOL JSM-6700F using accelerating voltages of 1.5−3 keV. Before observations, the samples were sputter-coated with 2−3 nm of platinum to avoid the charge effect (the platinum coating thickness was estimated from a calculated deposition rate and experimental deposition time). To further confirm the structure of the ordered bicontinuous TiO_2, we collected the powder of bicontinuous TiO_2 and performed a wide-angle X-ray diffraction (WAXS) experiment. The crystal structure of the as-prepared product was characterized by WAXS using a Rigaku D_{max} 2200 X-ray diffractometer with Cu KR radiation (λ = 0.1542 nm). The scanning 2θ angle ranged between 20° and 120° with step scanning of 1° for 1 s.

■ ASSOCIATED CONTENT

Ⓢ Supporting Information

Additional figures as described. This material is available free of charge via the Internet at http://pubs.acs.org.

■ AUTHOR INFORMATION

Corresponding Author

*Tel: 886-3-5738349; Fax: 886-3-5715408; e-mail: rmho@mx.nthu.edu.tw.

Notes

The authors declare no competing financial interest.

■ ACKNOWLEDGMENTS

The authors would like to thank the National Science Council of the Republic of China, Taiwan, for financially supporting this research under Contract No. Grant NSC 100-2120-M-007-013-. Ms. -H. Wu of the Department of Applied Chemistry at NCTU is appreciated for her assistance in the FESEM experiments, as well the National Synchrotron Radiation Research Center (NSRRC) for its assistance in the Synchrotron SAXS experiments.

■ REFERENCES

(1) Fleisher, R. L.; Price, P. B.; Walker, R. M. *Nuclear tracks in solids: principles and applications*; University of California Press: Berkeley, CA, 1975.

(2) Furneaux, R. C.; Rigby, W. R.; Davidson, A. P. The Formation of Controlled-Porosity Membranes from Anodically Oxidized Aluminum. *Nature* **1989**, *337*, 147−149.

(3) Zakhidov, A. A.; Baughman, R. H.; Iqbal, Z.; Cui, C. X.; Khayrullin, I.; Dantas, S. O.; Marti, I.; Ralchenko, V. G. Carbon Structures with Three-Dimensional Periodicity at Optical Wavelengths. *Science* **1998**, *282*, 897−901.

(4) Jiang, P.; Cizeron, J.; Bertone, J. F.; Colvin, V. L. Preparation of Macroporous Metal Films from Colloidal Crystals. *J. Am. Chem. Soc.* **1999**, *121*, 7957−7958.

(5) Monnier, A.; Schuth, F.; Huo, Q.; Kumar, D.; Margolese, D.; Maxwell, R. S.; Stucky, G. D.; Krishnamurty, M.; Petroff, P.; Firouzi, A.; Janicke, M.; Chmelka, B. F. Cooperative Formation of Inorganic-Organic Interfaces in the Synthesis of Silicate Mesostructures. *Science* **1993**, *261*, 1299−1303.

(6) Bates, F. S.; Fredrickson, G. H. Block Copolymer Thermodynamics: Theory and Experiment. *Annu. Rev. Phys. Chem.* **1990**, *41*, 525−557.

(7) Bates, F. S.; Fredrickson, G. H. Block Copolymers-Designer Soft Materials. *Phys. Today* **1999**, *52*, 32−38.

(8) Park, M.; Harrison, C.; Chaikin, P. M.; Register, R. A.; Adamson, D. H. Block Copolymer Lithography: Periodic Arrays of ∼1011 Holes in 1 Square Centimeter. *Science* **1997**, *276*, 1401−1404.

(9) Thurn-Albrecht, T.; Steiner, R.; DeRouchey, J.; Stafford, C. M.; Huang, E.; Bal, M.; Tuominen, M.; Hawker, C. J.; Russell, T. P. Nanoscopic Templates from Oriented Block Copolymer Films. *Adv. Mater.* **2000**, *12*, 787−791.

(10) Cheng, J. Y.; Ross, C. A.; Chan, V. Z. H.; Thomas, E. L.; Lammertink, R. G. H.; Vancso, G. J. Formation of a Cobalt Magnetic Dot Array *via* Block Copolymer Lithography. *Adv. Mater.* **2001**, *13*, 1174−1178.

(11) (a) Zalusky, A. S.; Olayo-Valles, R.; Taylor, C. J.; Hillmyer, M. A. Mesoporous Polystyrene Monoliths. *J. Am. Chem. Soc.* **2001**, *123*, 1519−1520. (b) Zalusky, A. S.; Olayo-Valles, R.; Wolf, J. H.; Hillmyer, M. A. Ordered Nanoporous Polymers from Polystyrene-Polylactide Block Copolymers. *J. Am. Chem. Soc.* **2002**, *124*, 12761−12773.

(12) (a) Ho, R. M.; Tseng, W. H.; Fan, H. W.; Chiang, Y.-W.; Lin, C. C.; Ko, B. T.; Huang, B. H. Solvent-Induced Microdomain Orientation in Polystyrene-*b*-Poly(l-lactide) Diblock Copolymer Thin Films for Nanopatterning. *Polymer* **2005**, *46*, 9362−9377. (b) Tseng, W. H.; Chen, C. K.; Chiang, Y. W.; Ho, R. M.; Akasaka, S.; Hasegawa, H. Helical Nanocomposites from Chiral Block Copolymer Templates. *J. Am. Chem. Soc.* **2009**, *131*, 1356−1357.

(13) Ho, R.-M.; Chiang, Y.-W.; Tsai, C. C.; Lin, C. C.; Ko, B. T.; Huang, H. B. H. Three-Dimensionally Packed Nanohelical Phase in Chiral Block Copolymers. *J. Am. Chem. Soc.* **2004**, *126*, 2704−2705.

(14) Hajduk, D. A.; Harper, P. E.; Gruner, S. M.; Honeker, C. C.; Kim, G.; Thomas, E. L.; Fetters, L. J. The gyroid: A New Equilibrium Morphology in Weakly Segregated Diblock Copolymers. *Macromolecules* **1994**, *27*, 4063−4075.

(15) Schulz, M. F.; Bates, F. S.; Almdal, K.; Mortensen, K. Epitaxial Relationship for Hexagonal-to-Cubic Phase Transition in a Book Copolymer Mixture. *Phys. Rev. Lett.* **1994**, *73*, 86−89.

(16) Matsen, M. W.; Schick, M. Stable and Unstable Phases of a Diblock Copolymer Melt. *Phys. Rev. Lett.* **1994**, *72*, 2660−2663.

(17) Martin-Moreno, L.; Garcia-Vidal, F. J.; Somoza, A. M. Self-Assembled Triply Periodic Minimal Surfaces as Molds for Photonic Band Gap Materials. *Phys. Rev. Lett.* **1999**, *83*, 73−75.

(18) Urbas, A. M.; Maldovan, M.; DeRege, P.; Thomas, E. L. Bicontinuous Cubic Block Copolymer Photonic Crystals. *Adv. Mater.* **2002**, *14*, 1850−1853.

(19) Hashimoto, T.; Tsutsumi, K.; Funaki, Y. Nanoprocessing Based on Bicontinuous Microdomains of Block Copolymers: Nanochannels Coated with Metals. *Langmuir* **1997**, *13*, 6869−6872.

(20) Chan, V.Z.-H.; Hoffman, J.; Lee, V. Y.; Latrou, H.; Avgeropoulos, A.; Hadjichristidis, N.; Miller, R. D.; Thomas, E. L. Ordered Bicontinuous Nanoporous and Nanorelief Ceramic Films from Self Assembling Polymer Precursors. *Science* **1999**, *286*, 1716−1719.

(21) Finnefrock, A. C.; Ulrich, R.; Toombes, G. E. S.; Gruner, S. M.; Wiesner, U. The Plumber's Nightmare: A New Morphology in Block Copolymer-Ceramic Nanocomposites and Mesoporous Aluminosilicates. *J. Am. Chem. Soc.* **2003**, *125*, 13084−13093.

(22) Jain, A.; Toombes, G. E. S.; Hall, L. M.; Mahajan, S.; Garcia, C. B. W.; Probst, W.; Gruner, S. M.; Wiesner, U. Direct Access to Bicontinuous Skeletal Inorganic Plumber's Nightmare Networks from Block Copolymers. *Angew. Chem., Int. Ed.* **2005**, *44*, 1226−1229.

(23) Crossland, E. J. W.; Kamperman, M.; Nedelcu, M.; Ducati, C.; Wiesner, U.; Smilgies, D. M.; Toombes, G. E. S.; Hillmyer, M. A.; Ludwigs, S.; Steiner, U.; Snaith, H. J. A Bicontinuous Double Gyroid Hybrid Solar Cell. *Nano Lett.* **2009**, *9*, 2807−2812.

(24) Adachi, M.; Okumura, A.; Sivaniah, E.; Hashimoto, T. Incorporation of Metal Nanoparticles into a Double Gyroid Network Texture. *Macromolecules* **2006**, *39*, 7352−7357.
(25) Urade, V. N.; Wei, T. C.; Tate, M. P.; Kowalski, J. D.; Hillhouse, H. W. Nanofabrication of Double-Gyroid Thin Films. *Chem. Mater.* **2007**, *19*, 768−777.
(26) Finnemore, A. S.; Scherer, M. R. J.; Langford, R.; Mahajan, S.; Ludwigs, S.; Meldrum, F. C.; Steiner, U. Nanostructured Calcite Single Crystals with Gyroid Morphologies. *Adv. Mater.* **2009**, *21*, 3928−3932.
(27) Ndoni, S.; Li, L.; Schulte, L.; Szewezykowski, P. P.; Hansen, T. W.; Guo, F. X.; Berg, R. H.; Vigild, M. E. Controlled Photooxidation of Nanoporous Polymers. *Macromolecules* **2009**, *42*, 3877−3880.
(28) Hsueh, H. Y.; Huang, Y. C.; Ho, R. M.; Lai, C. H.; Makida, T.; Hasegawa, H. Nanoporous Gyroid Nickel from Block Copolymer Templates *via* Electroless Plating. *Adv. Mater.* **2011**, *23*, 3041−3046.
(29) Hsueh, H. Y.; Chen, H. Y.; She, M. S.; Chen, C. K.; Ho, R. M.; Gwo, S.; Hasegawa, H.; Thomas, E. L. Inorganic Gyroid with Exceptionally Low Refractive Index from Block Copolymer Templating. *Nano Lett.* **2010**, *10*, 4994−5000.
(30) Vukovic, I.; Punzhin, S.; Vukovic, Z.; Onck, P.; De Hosson, J. T. M.; ten Brinke, G.; Loos, K. Supramolecular Route to Well-Ordered Metal Nanofoams. *ACS Nano* **2011**, *5*, 6339−6348.
(31) Scherer, M. R. J.; Li, L.; Cunha, P. M. S.; Scherman, O. A.; Steiner, U. Enhanced Electrochromism in Gyroid-Structured Vanadium Pentoxide. *Adv. Mater.* **2012**, *24*, 1217−1221.
(32) Vignolini, S.; Yufa, N. A.; Cunha, P. S.; Guldin, S.; Rushkin, I.; Stefik, M.; Hur, K.; Wiesner, U.; Baumberg, J. J.; Steiner, U. A 3D Optical Metamaterial Made by Self-Assembly. *Adv. Mater.* **2012**, *24*, OP23−OP27.
(33) Pierre, A. C. *Introduction to Sol-gel Processing*; Kluwer Academic: Boston, 1998.
(34) Hench, L. L.; West, J. K. The Sol-Gel Process. *Chem. Rev.* **1990**, *90*, 33−72.
(35) Grätzel, M. Photoelectrochemical Cells. *Nature* **2001**, *414*, 338−344.
(36) Adachi, M.; Murata, Y.; Harada, M.; Yoshikawa, Y. Formation of Titania Nanotubes with High Photo-Catalytic Activity. *Chem. Lett.* **2000**, *29*, 942−943.
(37) Chu, S. Z.; Inoue, S.; Wada, K.; Li, D.; Haneda, H.; Awatsu, S. Highly Porous $(TiO_2-SiO_2-TeO_2)/Al_2O_3/TiO_2$ Composite Nanostructures on Glass with Enhanced Photocatalysis Fabricated by Anodization and Sol−Gel Process. *J. Phys. Chem. B* **2003**, *107*, 6586−6589.
(38) Varghese, O. K.; Gong, D.; Paulose, M.; Ong, K. G.; Dickey, E. C.; Grimes, C. A. Extreme Changes in The Electrical Resistance of Titania Nanotubes with Hydrogen Exposure. *Adv. Mater.* **2003**, *15*, 624−627.
(39) Paulose, M.; Varghese, O. K.; Mor, G. K.; Grimes, C. A.; Ong, K. G. Unprecedented Ultra-High Hydrogen Gas Sensitivity in Undoped Titania Nanotubes. *Nanotechnology* **2006**, *17*, 398−402.
(40) Mor, G. K.; Shankar, K.; Paulose, M.; Varghese, O. K.; Grimes, C. A. Enhanced Photocleavage of Water Using Titania Nanotube Arrays. *Nano Lett.* **2005**, *5*, 191−195.
(41) Uchida, S.; Chiba, R.; Tomiha, M.; Masaki, N.; Shirai, M. Application of Titania Nanotubes to a Dye-Sensitized Solar Cell. *Electrochemistry* **2002**, *70*, 418−420.
(42) Mor, G. K.; Shankar, K.; Paulose, M.; Varghese, O. K.; Grimes, C. A. Use of Highly-Ordered TiO_2 Nanotube Arrays in Dye-Sensitized Solar Cells. *Nano Lett.* **2006**, *6*, 215−218.
(43) Paulose, M.; Shankar, K.; Varghese, O. K.; Mor, G. K.; Hardin, B.; Grimes, C. A. Backside Illuminated Dye-Sensitized Solar Cells Based on Titania Nanotube Array Electrodes. *Nanotechnology* **2006**, *17*, 1446−1448.
(44) Grätzel, M. Dye-Sensitized Solid-State Heterojunction Solar Cells. *MRS Bull.* **2005**, *30*, 23−27.
(45) Snaith, H. J.; Schmidt-Mende, L. Advances in Liquid-Electrolyte and Solid-State Dye-Sensitized Solar Cells. *Adv. Mater.* **2007**, *19*, 3187−3200.
(46) Tan, L. K.; Chong, M. A. S.; Gao, H. Free-Standing Porous Anodic Alumina Templates for Atomic Layer Deposition of Highly Ordered TiO_2 Nanotube Arrays on Various Substrates. *J. Phys. Chem. C* **2008**, *112*, 69−73.
(47) He, R. R.; Feng, X. L.; Roukes, M. L.; Yang, P. D. Self-Transducing Silicon Nanowire Electromechanical Systems at Room Temperature. *Nano Lett.* **2008**, *8*, 3781−3786.
(48) Kim, S. W.; Han, T. H.; Kim, J.; Gwon, H.; Moon, H. S.; Kang, S. W.; Kim, S. O.; Kang, K. Fabrication and Electrochemical Characterization of TiO_2 Three-Dimensional Nanonetwork Based on Peptide Assembly. *ACS Nano* **2009**, *3*, 1085−1090.
(49) Sauvage, F.; Di Fonzo, F.; Bassi, A. Li; Casari, C. S.; Russo, V.; Divitini, G.; Ducati, C.; Bottani, C. E.; Comte, P.; Graetzel, M. Hierarchical TiO_2 Photoanode for Dye-Sensitized Solar Cells. *Nano Lett.* **2010**, *10*, 2562−2567.
(50) Ghadiri, E.; Taghavinia, N.; Zakeeruddin, S. M.; Gräetzel, M.; Moser, J.-E. Enhanced Electron Collection Efficiency in Dye-Sensitized Solar Cells Based on Nanostructured TiO_2 Hollow Fibers. *Nano Lett.* **2010**, *10*, 1632−1638.
(51) Livage, J.; Henry, M.; Sanchez, C. Sol-Gel Chemistry of Transition Metal Oxides. *Prog. Solid State Chem.* **1988**, *18*, 259−341.
(52) Chen, X.; Mao, S. S. Titanium Dioxide Nanomaterials: Synthesis, Properties, Modifications, and Applications. *Chem. Rev.* **2007**, *107*, 2891−2959.
(53) Carp, O.; Huisman, C. L.; Reller, A. Photoinduced Reactivity of Titanium Dioxide. *Prog. Solid State Chem.* **2004**, *32*, 33−177.
(54) Sing, K. S. W.; Everett, D. H.; Haul, R. A. W.; Moscou, L.; Pierotti, R. A.; Rouquerol, J.; Siemieniewska, T. Reporting Physisorption Data for Gas/Solid Systems. *Pure Appl. Chem.* **1985**, *57*, 603−619.